

# Non-Newtonian effects on draw resonance in film casting

M. Bechert

*Forschungszentrum Jülich, Helmholtz Institute Erlangen-Nürnberg for Renewable Energy (IEK-11), Fürther Straße 248, 90429 Nürnberg, Germany*

---

## Abstract

In this paper, the influence of non-Newtonian material properties on the draw resonance instability in film casting is investigated. Viscoelastic models of infinite width film casting are derived systematically following an asymptotic expansion and using three well-known constitutive equations: the upper-convected Maxwell model, the Giesekus model, and the simplified Phan-Thien–Tanner model. Based on a steady state analysis, a numerical boundary condition for the inlet stresses is formulated, which suppresses the unknown deformation history of the die flow. The critical draw ratio in dependence of both the Deborah number and the nonlinear parameters is calculated by means of linear stability analysis. For the Giesekus and PTT models, the most unstable instability mode may switch for different control parameters, leading to a non-continuous change in the oscillation frequency at criticality. The effective elongational viscosity, which depends exclusively on the local Weissenberg number, is analyzed and identified as crucial quantity as long as the Deborah number is not too large. This is demonstrated by using generalized Newtonian fluid models to approximate the viscoelastic models. Based on these generalized Newtonian fluid models, the effects of strain hardening and strain thinning are finally explored, revealing two opposing mechanisms underlying the non-Newtonian stability behavior.

---

## 1. Introduction

In film casting processes, molten material is extruded through a slit die, here referred to as the inlet, and taken-up by a distant, rotating chill roll, here referred to as the outlet (see Fig. 1(a)). Usually, the rotation speed at the outlet is desired to be high in order to produce films of preferably small height. The so-called draw resonance instability imposes an upper bound on the draw ratio, which is defined as the ratio of outlet to inlet velocity, and manifests itself in steady oscillations of flow velocity and both film thickness and width [1]. Many

---

*Email address:* `m.bechert@fz-juelich.de` (M. Bechert)

theoretical studies on this phenomenon were undertaken in the past decades, starting with a linear stability analysis of a purely viscous, one-dimensional model for infinite width film casting of a Newtonian fluid [2]. This model had been extended afterwards in several works to cover additional effects like inertia and gravity [3, 4], neck-in [5, 6], and cooling [7].

In many cases, viscoelastic materials like polymer melts are processed and the non-Newtonian flow properties need to be respected in the modeling. First attempts were made employing a power-law equation in generalized Newtonian fluid (GNF) models [8, 9, 10]. A power-law index larger than unity, i.e., pure strain hardening, was found to increase the critical draw ratio, while an index below unity, i.e., pure strain thinning, decreases the stability as compared to the well-known Newtonian value of 20.218. Silagy et al. [5] investigated the linear stability analysis of an upper-convected Maxwell (UCM) fluid. A strongly stabilizing effect of increasing Deborah number is predicted, including a second critical draw ratio beyond which the process becomes stable again. Moreover, an unattainable region for high Deborah numbers and draw ratios is reported, where no steady state solutions exist.

Stability studies utilizing the Phan-Thien/Tanner (PTT) [11, 12] and the eXtended Pom-Pom model [13, 14] constitutive equations reveal in contrast to that a mostly destabilizing effect of increasing elastic properties of the material, which is in qualitative agreement with experimental findings [15, 16]. Iyengar and Co [17, 18] performed a steady state and a linear stability analysis of one-dimensional, infinite width film casting of a modified Giesekus fluid. The results are correlated with the dependence of the steady shear and uniaxial elongational viscosities on the deformation rates and shear thinning is found to lead to destabilization, while strain hardening can lead to a stabilization depending on the range of relaxation time and strain rates occurring within the process. While all of the above mentioned studies employ single mode models, there exist up to now also two works on draw resonance for a multi-relaxation-mode PTT model [19, 20].

Even though many investigations on draw resonance can be found, including viscoelastic effects, some fundamental questions remain still unanswered. First of all, the influences of non-Newtonian, viscous effects and purely elastic effects on the critical draw ratio are not well separated yet. This includes the question, whether a GNF model is sufficient for essentially predicting the critical draw ratio. While Iyengar and Co [18] attempted to investigate the stability mechanism of a deformation dependent viscosity, their analysis suffers from two major drawbacks: They used the uniaxial elongational viscosity, while the one-dimensional film casting process is governed exclusively by planar deformation, and they neglected the time dependence of the viscosity by accounting for the steady values, which are valid only for sufficiently long lasting deformations at constant deformation rate. For these reasons, it is still unclear if strain hardening (strain thinning) always leads to stabilization (destabilization) and why (not). Moreover, the qualitative difference of the stabilizing influence of elasticity as predicted by the UCM model on the one side, and the opposite predictions of other viscoelastic models on the other side has not been explained up to now,

which is strongly connected to the minimum requirements for a constitutive equation to yield at least qualitative coincidence with experimental findings. The present study aims to address these questions, as well as to provide a comprehensive and consistent picture of the stability behavior of the commonly most used viscoelastic models.

The paper is organized as follows. We start with the derivation of the one-dimensional models following an asymptotic expansion of the flow equations in Sec. 2. We will use a uniform notation which enables us to use the same equations for all three employed constitutive equations by simply tuning the corresponding parameters. For a first start, an empirical stress boundary condition will be defined. Then, a steady state analysis is performed in Sec. 3, which primarily serves the purpose of refining the stress boundary condition in a more consistent, physical way. Afterwards, the linear stability equations are derived and the stability results are presented in Sec. 4 for all three constitutive equations. We then focus on non-Newtonian, viscous models in Sec. 5 and analyze in particular the effective elongational viscosity. Based on this quantity, we test the possibility to approximate the previously studied viscoelastic models by GNF models, and discuss the limitations of this approach. Finally, the mechanisms underlying the stability behavior of strain hardening and strain thinning materials are revealed in Sec. 6. The paper closes with brief conclusions and outlook.

## 2. The model

### 2.1. Governing equations

The infinite width film casting model as presented by Yeow [2] will be extended to viscoelastic constitutive equations. For this purpose, an asymptotic expansion in a small film parameter will be employed to obtain the one-dimensional equations at leading order, following previous studies on Newtonian fluids [6, 7]. Figure 1(b) shows a sketch of the film model between inlet and outlet. Assuming an infinite width of the film, it is sufficient to analyze the cross section of the film in the  $xy$ -plane, which is described by the film thickness  $h(x, t)$  and the casting length  $L$ . The velocity field is denoted by  $\mathbf{v} = (u, v)$ , with axial velocity  $u$  and transversal velocity  $v$ , and  $t$  denotes the time. At the inlet, axial velocity and thickness are prescribed by the extrusion to  $u_0$  and  $h_0$ , respectively. At the outlet, the axial velocity is fixed by the take-up with the chill roll to  $u_L = Dr u_0$ , where the draw ratio  $Dr$  is introduced as primary control parameter.

The continuity and momentum conservation equations, given by, respectively,

$$\nabla \cdot \mathbf{v} = 0, \quad (1a)$$

$$\nabla \cdot \boldsymbol{\sigma} = 0, \quad (1b)$$

with  $\nabla = (\partial_x, \partial_y)$  and stress tensor  $\boldsymbol{\sigma}$ , are coupled to the general constitutive equation

$$\lambda \nabla \cdot \boldsymbol{\tau} + \mathbf{Y}(\boldsymbol{\tau}) = \eta_0 (\nabla \mathbf{v} + (\nabla \mathbf{v})^T), \quad (2)$$

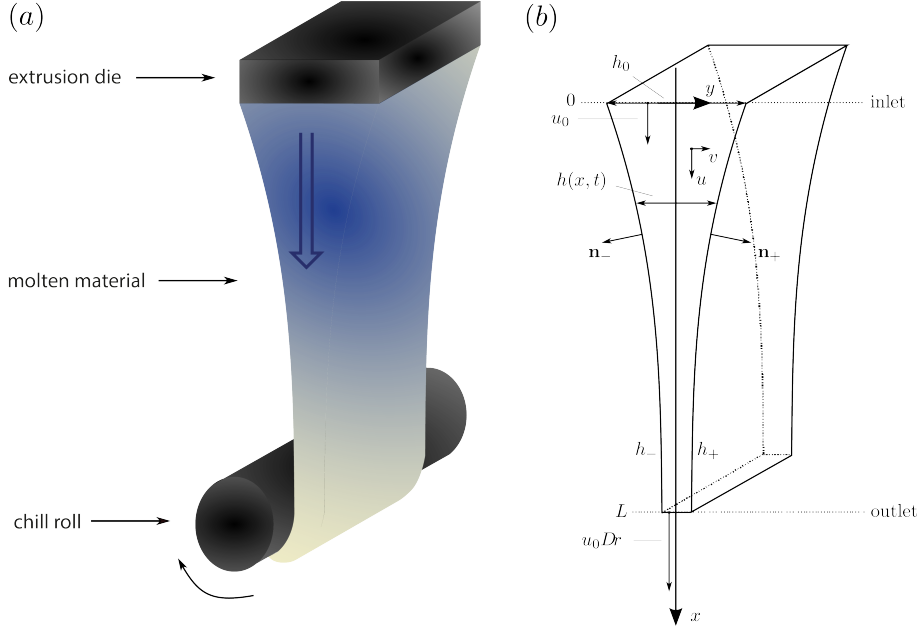


Figure 1: (a) Sketch of the film casting process. The flow direction is indicated with a big arrow. (b) Sketch of the one-dimensional model for an infinitely wide film.

with upper-convected time derivative

$$\frac{\nabla}{\tau} = \partial_t \tau + \mathbf{v} \cdot \nabla \tau - \tau \cdot \nabla \mathbf{v} - (\nabla \mathbf{v})^T \cdot \tau \quad (3)$$

of the extra stress tensor  $\tau = p\mathbf{1} + \boldsymbol{\sigma}$ ,  $p$  denoting the pressure.  $\lambda$  is the relaxation time and  $\eta_0$  the zero-shear viscosity, both assumed to be constant. The auxiliary tensor  $\mathbf{Y}$  is defined as

$$\mathbf{Y}(\tau) = \begin{cases} \tau & \text{for the UCM model,} \\ \tau + \alpha \frac{\lambda}{\eta_0} \tau^2 & \text{for the Giesekus model,} \\ \exp\left(\varepsilon \frac{\lambda}{\eta_0} \text{tr}(\tau)\right) \tau & \text{for the PTT model,} \end{cases} \quad (4)$$

$\text{tr}(\tau)$  denoting the trace of  $\tau$ . The Giesekus and PTT models [21] introduce an additional, nonlinear parameter denoted by  $\alpha$  or, respectively,  $\varepsilon$ . Note that only the so-called simplified PTT model with one nonlinear parameter is treated in this paper. In the following, we will shorten the notation by combining the three models with the note that the nonlinear parameters  $\alpha$  and  $\varepsilon$  have to be set to zero depending on the chosen model, i.e.,

$$\mathbf{Y}(\tau) = \exp\left(\varepsilon \lambda / \eta_0 \text{tr}(\tau)\right) \tau + \alpha \lambda / \eta_0 \tau^2. \quad (5)$$

At the free surfaces  $h_{\pm}$  defined by  $y = \pm h/2$ , the kinematic and stress boundary conditions,

$$\partial_t h_{\pm} + u|_{h_{\pm}} \partial_x h_{\pm} - v|_{h_{\pm}} = 0, \quad (6a)$$

$$\mathbf{n}_{\pm} \cdot \boldsymbol{\sigma}|_{h_{\pm}} = 0, \quad (6b)$$

with normal vector  $\mathbf{n}_{\pm} = (-\partial_x h_{\pm}, 1)/\sqrt{1 + (\partial_x h)^2/4}$ , are imposed.

## 2.2. Scaling and asymptotic expansion

The system is scaled according to the following transformations,

$$\begin{aligned} x &\rightarrow Lx, \quad y \rightarrow \beta Ly, \quad u \rightarrow u_0 u, \quad v \rightarrow \beta u_0 v, \\ h &\rightarrow \beta L h, \quad t \rightarrow \frac{L}{u_0} t, \quad \boldsymbol{\tau} \rightarrow \eta \frac{u_0}{L} \boldsymbol{\tau}, \quad p \rightarrow \eta \frac{u_0}{L} p, \quad \boldsymbol{\sigma} \rightarrow \eta \frac{u_0}{L} \boldsymbol{\sigma}, \end{aligned} \quad (7)$$

with the film parameter  $\beta = h_0/L$  assumed to be small. From now on, only scaled variables will be used unless explicitly stated differently.

The continuity equation (1a) can then be written,

$$\partial_x u + \partial_y v = 0, \quad (8)$$

and the two components of the momentum conservation (1b) become

$$\beta^2 \partial_x \sigma_{xx} + \partial_y \sigma_{xy}^* = 0, \quad (9a)$$

$$\partial_x \sigma_{xy}^* + \partial_y \sigma_{yy} = 0, \quad (9b)$$

with  $\sigma_{xy}^* = \beta \sigma_{xy}$ . The components of the stress boundary condition (6b) read

$$-\beta^2 \partial_x h_{\pm} \sigma_{xx}|_{h_{\pm}} + \sigma_{xy}^*|_{h_{\pm}} = 0, \quad (10a)$$

$$-\partial_x h_{\pm} \sigma_{xy}^*|_{h_{\pm}} + \sigma_{yy}|_{h_{\pm}} = 0, \quad (10b)$$

and the constitutive equation (2) is given by

$$\begin{aligned} D\epsilon (\beta^2 (\partial_t \tau_{xx} + u \partial_x \tau_{xx} + v \partial_y \tau_{xx}) \\ - 2 (\beta^2 \tau_{xx} \partial_x u + \tau_{xy}^* \partial_y u)) + Y_{xx} = 2 \beta^2 \partial_x u, \end{aligned} \quad (11a)$$

$$\begin{aligned} \beta^2 D\epsilon (\partial_t \tau_{yy} + u \partial_x \tau_{yy} + v \partial_y \tau_{yy} - \\ 2 (\tau_{yy} \partial_y v + \tau_{xy}^* \partial_x v)) + Y_{yy} = 2 \beta^2 \partial_y v, \end{aligned} \quad (11b)$$

$$\begin{aligned} D\epsilon (\partial_t \tau_{xy}^* + u \partial_x \tau_{xy}^* + v \partial_y \tau_{xy}^* - \tau_{xy}^* \partial_y v \\ - \beta^2 \tau_{xx} \partial_x v - \tau_{xy}^* \partial_x u - \tau_{yy} \partial_y u) + Y_{xy} = \beta^2 \partial_x v + \partial_y u, \end{aligned} \quad (11c)$$

where  $\tau_{xy}^* = \beta \tau_{xy}$ , and with Deborah number  $D\epsilon = \lambda u_0/L$  and

$$Y_{xx} = \beta^2 \tau_{xx} \exp [\varepsilon D\epsilon (\tau_{xx} + \tau_{yy})] + \alpha D\epsilon (\beta^2 \tau_{xx}^2 + \tau_{xy}^{*2}), \quad (12a)$$

$$Y_{yy} = \beta^2 \tau_{yy} \exp [\varepsilon D\epsilon (\tau_{xx} + \tau_{yy})] + \alpha D\epsilon (\beta^2 \tau_{yy}^2 + \tau_{xy}^{*2}), \quad (12b)$$

$$Y_{xy} = \tau_{xy}^* \exp [\varepsilon D\epsilon (\tau_{xx} + \tau_{yy})] + \alpha D\epsilon (\beta^2 \tau_{yy}^2 + \tau_{xy}^{*2}). \quad (12c)$$

The stresses, pressure, and velocity variables are now expanded in the square film parameter  $\beta^2$ , i.e., for any variable  $\phi \in \{u, v, p, \boldsymbol{\tau}, \boldsymbol{\sigma}\}$ ,

$$\phi = \phi^{(0)} + \beta^2 \phi^{(1)} + \mathcal{O}(\beta^4). \quad (13)$$

Equations (9a) and (10a) truncated at  $\mathcal{O}(\beta^2)$  then lead to  $\sigma_{xy}^{*(0)} = \tau_{xy}^{*(0)} = 0$ , and therefore Eq. (11c) yields

$$\left(De \tau_{yy}^{(0)} + 1\right) \partial_y u^{(0)} = 0 \quad (14)$$

at leading order. Assuming  $\partial_y u^{(0)}$  being non-zero would directly lead to

$$\tau_{yy}^{(0)} = -\frac{1}{De}, \quad (15)$$

which implies that the transversal stress component diverges in the case of the Newtonian limit  $De \rightarrow 0$ . As this is obviously not the case, the only consistent way to fulfill Eq. (14) is  $\partial_y u^{(0)} = 0$ , i.e., the axial velocity depends only on  $x$  and  $t$  at leading order.

### 2.3. Averaged equations

Averaging the continuity equation (8) at leading order over the thickness  $h$ , together with employing the kinematic boundary condition<sup>1</sup> (6a), we obtain the one-dimensional form of the continuity equation,

$$\partial_t h + \partial_x \left( h u^{(0)} \right) = 0. \quad (16)$$

Equations (9b) and (10b) yield  $\sigma_{yy}^{(0)} = 0$ , which makes  $\sigma_{xx}^{(0)}$  equal to the normal stress difference  $\nu^{(0)} = \tau_{xx}^{(0)} - \tau_{yy}^{(0)}$  at leading order. Averaging the  $x$ -component of the momentum equation (9a) over the film thickness by utilizing the first order solution at the boundaries  $\sigma_{xy}^{*(1)}$  as obtained from Eq. (10a) finally leads therefore to

$$\partial_x \left( h \overline{\nu^{(0)}} \right) = 0, \quad (17)$$

with the depth-averaged normal stress difference at leading order given by

$$\overline{\nu^{(0)}} = \frac{1}{h} \int_{-h/2}^{h/2} dy \nu^{(0)}. \quad (18)$$

Finally, the first non-vanishing order of Eqs. (11a) and (11b) is averaged along the film thickness. While this step is rather straight-forward in the case of the UCM model, we have to assume additionally

$$\left| \tau_{ii}^{(0)} - \overline{\tau_{ii}^{(0)}} \right| = \mathcal{O}(\beta), \quad (19)$$

---

<sup>1</sup>The kinematic boundary condition remains unchanged by the scaling transformation.

for the Giesekus and PTT models, as this ensures that we can calculate the average of nonlinear stress terms at leading order by

$$\frac{1}{h} \int_{-h/2}^{h/2} dy \left( \overline{\tau_{ii}^{(0)}} \right)^2 = \left( \overline{\tau_{ii}^{(0)}} \right)^2. \quad (20)$$

Employing the continuity equation (8), one then obtains

$$De \left[ \partial_t \overline{\nu^{(0)}} + u^{(0)} \partial_x \overline{\nu^{(0)}} + 2 \partial_x u^{(0)} \left( \overline{\nu^{(0)}} - 2 \overline{\tau_{xx}^{(0)}} \right) \right] + Z_\nu \overline{\nu^{(0)}} = 4 \partial_x u^{(0)}, \quad (21a)$$

$$De \left( \partial_t \overline{\tau_{xx}^{(0)}} + u^{(0)} \partial_x \overline{\tau_{xx}^{(0)}} - 2 \partial_x u^{(0)} \overline{\tau_{xx}^{(0)}} \right) + Z_{xx} \overline{\tau_{xx}^{(0)}} = 2 \partial_x u^{(0)}, \quad (21b)$$

with

$$Z_\nu = \exp \left[ \varepsilon De \left( 2 \overline{\tau_{xx}^{(0)}} - \overline{\nu^{(0)}} \right) \right] + \alpha De \left( 2 \overline{\tau_{xx}^{(0)}} - \overline{\nu^{(0)}} \right), \quad (22a)$$

$$Z_{xx} = \exp \left[ \varepsilon De \left( 2 \overline{\tau_{xx}^{(0)}} - \overline{\nu^{(0)}} \right) \right] + \alpha De \overline{\tau_{xx}^{(0)}}, \quad (22b)$$

where a generalized version of Eq. (20) was used to average the exponential term of the PTT model.

Equations (16), (17) and (21) determine the evolution of the four state variables  $u^{(0)}$ ,  $h^{(0)}$ ,  $\overline{\nu^{(0)}}$  and  $\overline{\tau_{xx}^{(0)}}$ . We will omit the averaging bar and the superscript “(0)” from now on and simply use  $u$ ,  $h$ ,  $\nu$  and  $\tau_{xx}$  for the variables at leading order. Nevertheless, it is important to point out that, in contrast to the Newtonian model, the stress components are not necessarily identical to their averaged quantities. This is usually ignored in the present literature and the equations are mostly derived by assuming *a-priori* transversal invariance of the variables as well as neglecting off-diagonal stress components.

#### 2.4. Boundary conditions (empirical approach)

Three boundary conditions are given directly by the process setup,

$$u(x = 0, t) = h(x = 0, t) = 1, \quad (23a)$$

$$u(x = 1, t) = Dr. \quad (23b)$$

With four first-order differential equations (16), (17) and (21), a fourth spatial boundary condition is needed. This one is physically determined by the pre-history of the flow in the die, which defines the stress components at the inlet. A comprehensive analysis including the die flow increases significantly the complexity of the problem, which is why we will follow an alternative approach here. As already pointed out by Papanastasiou et al. [22] for fiber spinning, the ratio of transversal stress to the normal stress difference decreases monotonically with increasing elastic effects. At the Newtonian limit, i.e.,  $De \rightarrow 0$ , the value is fixed

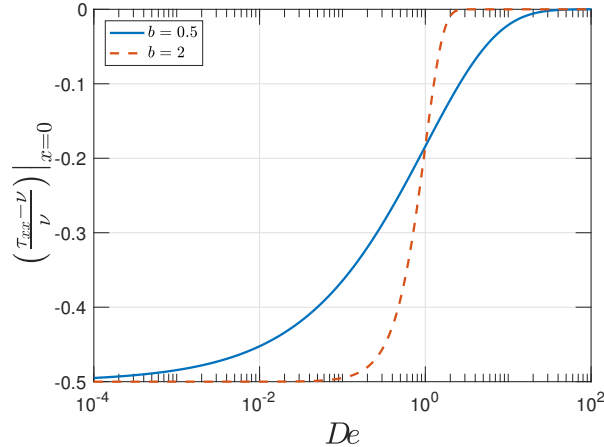


Figure 2: Empirical stress boundary condition (24) for  $b = 0.5$  and  $2$ .

to  $\tau_{yy}/\nu = -1/2$  and in the elastic limit, i.e.,  $De \rightarrow \infty$ , the transversal stress vanishes. Papanastasiou et al. [22] proposed a so-called free boundary condition method to define implicitly a stress inlet condition using finite element methods. This boundary condition is equivalent to assuming that the deformation in the die is exactly the same as outside the die, i.e., purely extensional, and leads therefore to smooth stress profiles without boundary layers at the inlet. Here, we will introduce a rather empirical, but more flexible approach, which will be elaborated completely in Sec. 3.3. For now, a qualitative expression based on the physical considerations above is used to obtain first results,

$$\left. \left( \frac{\tau_{xx} - \nu}{\nu} \right) \right|_{x=0} = -\frac{1}{2} \exp(-De^b), \quad (24)$$

which tunes the transversal stress  $\tau_{yy} = \tau_{xx} - \nu$  at the inlet exponentially from the Newtonian limit to zero with increasing Deborah number. The transition can be adjusted by parameter  $b$ , as it is depicted in Fig. 2 for two values of  $b$ .

### 3. Steady state analysis

#### 3.1. Steady state equations

The steady state equations, which determine the evolution of the time-independent solutions, can be obtained by neglecting the time derivatives in Eqs. (16), (17) and (21). This leads to the following system,

$$u'_s = \frac{\nu_s}{\tilde{\mu}_s}, \quad (25a)$$

$$h'_s = -\frac{h_s \nu_s}{u_s \tilde{\mu}_s}, \quad (25b)$$

$$\nu'_s = \nu_s \frac{u'_s}{u_s}, \quad (25c)$$

$$t'_s = \frac{1}{De u_s} [2 u'_s (1 + De t_s) - t_s Z_{xx,s}], \quad (25d)$$

where we introduce the *effective elongational viscosity* at steady state,

$$\tilde{\mu}_s = \frac{\nu_s}{u'_s} = \frac{4}{Z_{\nu,s}} \left[ 1 + De \left( t_s - \frac{3}{4} \nu_s \right) \right], \quad (26)$$

which will be investigated in more detail in Sec. 5. The steady state variables are indicated by a subscript ‘s’ and  $t_s = \tau_{xx,s}$  is used for the sake of convenience. Equations (25) are solved by numerical continuation employing the software AUTO-07P[23], using the Newtonian limit as an initial solution.

#### 3.2. Influence of stress boundary condition

Figure 3 depicts the steady state solutions for all three models for two Deborah numbers and two values of parameter  $b$ . For the UCM model we need to restrict the analysis to rather small Deborah numbers, as no steady state solutions exist for larger values [24]. The nonlinear parameters of the Giesekus and PTT models were set to  $\alpha = 0.3$  and  $\varepsilon = 0.3$ , respectively.

For all three models, the velocity and thickness profiles appear to be rather independent of the inlet stress condition. However, the transversal stress component changes significantly close to the die with varying initial conditions. With increasing  $x$ , the solutions approach each other and seem to be independent of the boundary condition. This was already reported before for the case of fiber spinning of a XPP fluid [13] and can be understood as a fading memory of the deformation pre-history in the die, which leads to the particular inlet stress condition. This transition occurs within a characteristic time reasonably linked to the relaxation time of the material, which in turn corresponds to a spatial position, as the time within which a fluid element has already experienced deformation can be linked to its position using the velocity profile, i.e.,  $dt = dx/v$ . For  $x \gg De$ , i.e., exceeding the characteristic time, the pre-history of deformation does not influence the transversal stress any more and is exclusively determined by the deformation outside the die. Note that this effect is not visible in the normal stress difference  $\nu_s$  and the axial stress component  $t_s$ , which are almost independent of the initial stress condition.

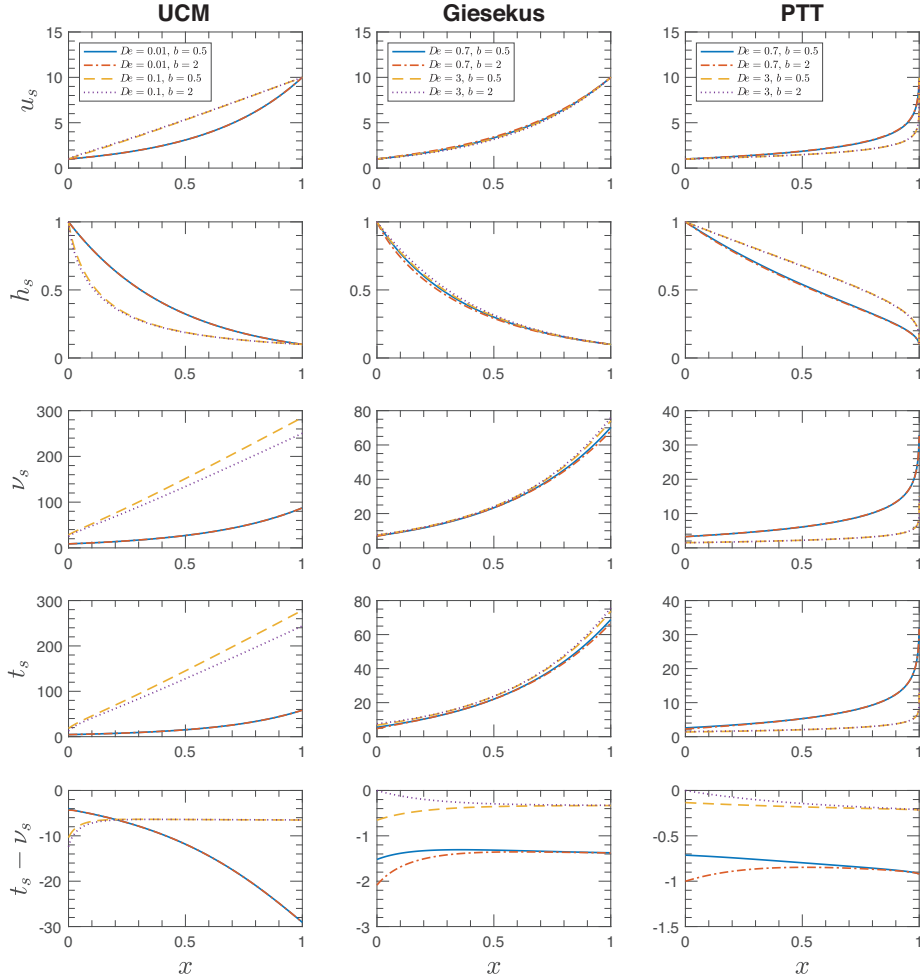


Figure 3: Steady state solutions for the UCM, Giesekus and PTT models employing the empirical inlet stress boundary condition (24) for  $b = 0.5$  and 2 at two Deborah numbers, with  $Dr = 10$ . Note that for the UCM model, only small values of  $De$  are shown as no steady solutions exist for larger values. For the Giesekus model  $\alpha = 0.3$  and for the PTT model  $\varepsilon = 0.3$ .

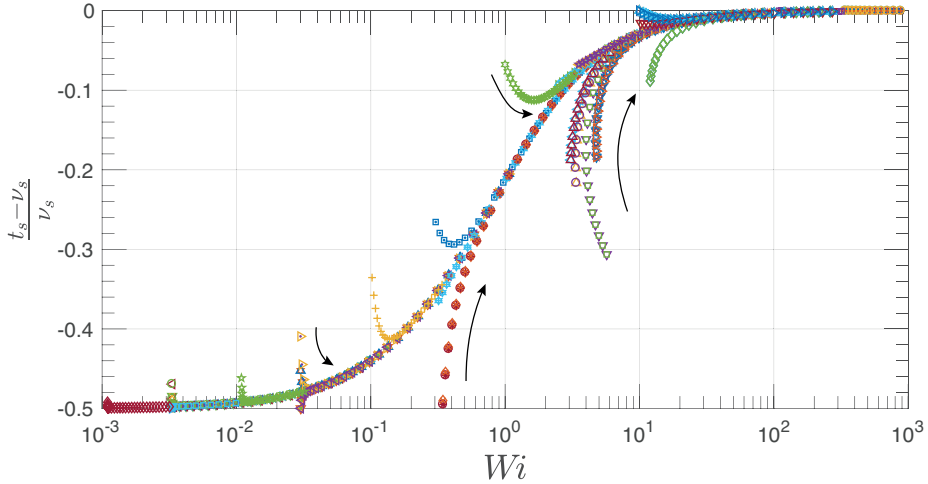


Figure 4: Ratio of transversal stress to normal stress difference as a function of the Weissenberg number for the Giesekus model with  $\alpha = 0.3$ , using the empirical boundary condition (24) with various values of  $b$ . Every data set corresponds to a particular draw ratio and a point-wise evaluation along the  $x$ -axis. The arrows indicate the increasing  $x$ -position, i.e., increasing time.

### 3.3. Refined stress boundary condition

Following the idea that there exists a characteristic length of transition after which the deformation is independent of the initial stress condition, we plot the transversal stress profile as a function of the Weissenberg number  $Wi = De \partial_x u$ , by evaluating both quantities point-wise along  $x$ . The result is shown by Fig. 4 for the Giesekus model with  $\alpha = 0.3$ . Every single curve corresponds to a different draw ratio, with various values of  $b$  in the inlet stress condition (24) and arrows indicating the direction of increasing  $x$ -position. It can be seen that with increasing  $x$ , i.e., with the fluid propagating towards the outlet, all curves collapse to a common mastercurve, which appears to be independent of the draw ratio. Similar behavior is also observed for the UCM and PTT models, including various values of nonlinear parameters.

The mastercurve for a particular model and nonlinear parameter value is obtained by truncating the transition regime, followed by numerical interpolation. Figure 5 depicts several of these mastercurves for the UCM, Giesekus and PTT models. Using this mastercurve, we now can define an initial stress condition based on the physical assumption that the pre-deformation occurring in the die is of the same type as between inlet and outlet, i.e., a planar elongation with varying strain rate. While this assumption may be questionable regarding the different flow properties inside and outside the die, it is still a reasonable one if we want to decouple the effect of die flow as much as possible from the actual casting deformation. In particular, it is identical to the free boundary condition presented by Papanastasiou et al. [22]. Another possibility would be to follow Barborik et al. [25], who used the fully developed flow profile

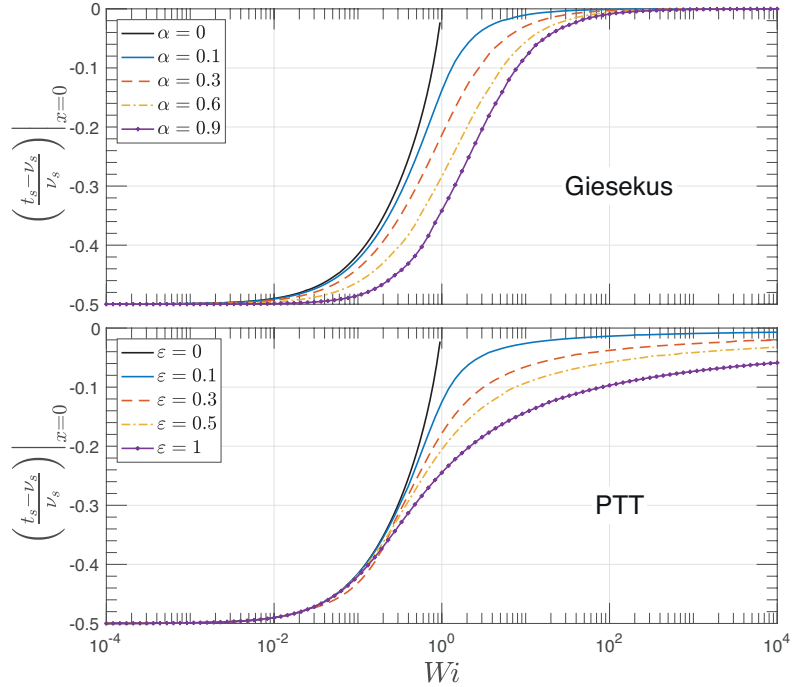


Figure 5: Mastercurves of the transversal stress as a function of the Weissenberg number for the Giesekus and PTT model for several nonlinear parameter values. The curves are obtained by numerical interpolation of the data obtained using initial stress condition (24), after it is truncated by the transition regime close to the inlet. The limit of the UCM model ( $\alpha, \varepsilon \rightarrow 0$ ) is not accessible for large Weissenberg numbers, as no steady state solutions exist.

in a rectangular channel to obtain the initial stress condition. This approach, however, increases the computational complexity significantly and introduces additional parameters for the channel. For the rest of this paper, boundary condition (24) is replaced by setting the transversal stress to the value obtained from the interpolated mastercurve.

#### 4. Linear stability analysis

##### 4.1. Perturbation equations

In order to determine the critical parameters beyond which draw resonance occurs, the following ansatz for the variables is posed,

$$\mathbf{v}(x, t) = \mathbf{v}_s(x) + \delta \sum_{n=0}^{\infty} \left( \mathbf{V}_n(x) e^{\omega_n t} + \mathbf{V}_n^*(x) e^{\omega_n^* t} \right), \quad (27)$$

which splits up the state vector  $\mathbf{v} = (u, h, \nu, t)$  into the steady state and a time dependent perturbation part, which is decomposed into perturbation modes

with complex perturbation  $\mathbf{V}_n = (u_s U_n, h_s H_n, \nu_s N_n, t_s T_n)$ , and corresponding complex eigenvalue  $\omega_n = \omega_{n,R} + i \omega_{n,I}$ . The real part  $\omega_{n,R}$  denotes the growth rate and the imaginary part  $\omega_{n,I}$  the frequency. The asterisk denotes the complex conjugate. The growth rate determines the stability of the mode, as  $\omega_{n,R} > 0$  leads to an exponential amplification of an initial perturbation, i.e., unstable behavior, and  $\omega_{n,R} < 0$  leads to an exponential damping, i.e., stable behavior. We focus on infinitesimal small perturbations only by letting  $\delta \ll 1$ . Ansatz (27) is plugged in Eqs (16), (17) and (21), keeping only terms linear in  $\delta$ . This linearization enables us to decouple the perturbation modes and each mode is determined by the same system of differential equations,

$$U' = \frac{u'_s}{u_s} \left[ N - U + \frac{De}{Z_{\nu,s}} \left( (\omega H + (\omega + 3u'_s - \nu_s(\alpha + \varepsilon Z_{\nu,s}))N) - 2t_s \left( \frac{2}{\tilde{\mu}_s} - (\alpha + \varepsilon Z_{\nu,s}) \right) T \right) \right], \quad (28a)$$

$$H' = - \left( \frac{\omega}{u_s} H + U' \right), \quad (28b)$$

$$N' = -H', \quad (28c)$$

$$T' = \frac{1}{De u_s t_s} [t_s Z_{xx,s} U + 2u_s (1 + De t_s) U' + \varepsilon De \nu_s t_s Z_{xx,s} N - (2u'_s + De t_s (\omega + t_s(\alpha + 2\varepsilon Z_{xx,s}))) T], \quad (28d)$$

which constitutes a homogeneous eigenvalue problem typical for linear stability analysis. Note that we omit the index ‘ $n$ ’ from now on for the sake of convenience. The critical draw ratio  $Dr_c$  and the frequency at criticality  $\omega_{I,c}$  are determined by the neutral stability condition  $\omega_R = 0$ , where we focus on the most unstable mode, i.e., largest  $\omega_R$ .

The boundary conditions for system (28) are dictated by conditions (23) and the prescription of the transversal stress at the inlet. As all these equations are time independent, the corresponding perturbations must vanish at these positions. Additionally, as system (28) is homogeneous, we need to specify the amplitude of perturbations. This choice is arbitrary and does not influence the stability predictions. Following previous work [6, 26], we fix the perturbation of the force at the outlet, so that the boundary conditions read

$$U(0) = H(0) = t_s(0)T(0) - \nu_s(0)N(0) = 0, \quad (29a)$$

$$U(1) = 0, \quad (29b)$$

$$H(1) + N(1) = 0.1. \quad (29c)$$

#### 4.2. Solution methods

The perturbation equations are solved by two distinct methods. The first consists, analogue to the solution of the steady state equations, in a numerical continuation with AUTO-07P[23], but this time with three continuation parameters as the real and imaginary parts of the eigenvalue increase the degree of

freedom by two. The procedure is to fix  $\alpha$  and  $\varepsilon$  to the desired values and to start with the solution in the Newtonian limit  $D\epsilon \rightarrow 0$ , for which an analytical expression exists [27]. The critical conditions are then found by varying  $Dr$ ,  $\omega_R$ , and  $\omega_I$  simultaneously until  $\omega_R = 0$ . Afterwards,  $\omega_R = 0$  is fixed and the Deborah number is used as primary continuation parameter, together with  $Dr_c$  and  $\omega_{I,c}$  as secondary parameters, following the neutral stability curve in the parameter space.

Despite its simple implementation and high computational efficiency, this method has one major drawback. It is tacitly assumed that the most unstable mode of the Newtonian limit remains the most unstable for all configurations, i.e., the frequency at criticality changes continuously under variation of the control parameters. As shown in the following, however, this is not always the case. We will therefore determine additionally the eigenvalue spectrum of Eqs. (28) to determine possible changes in the most unstable mode. For this purpose, the system is discretized with a Chebyshev collocation method utilizing the CHEBFUN [28] framework for MATLAB and the eigenvalues and eigenfunctions are computed with the intrinsic solver. In contrast to the method of numerical continuation, the critical conditions have to be found by manually stepping through the parameter space to find the neutral configuration of zero growth rate. Here we use a minimum incremental step size of 0.1 for the critical draw ratio, leading to an accuracy of  $\pm 0.05$ . As this procedure increases the computational effort and decreases the accuracy, this method is mostly used to verify, and if necessary correct, the results obtained by numerical continuation.

#### 4.3. UCM model

Figure 6 shows the critical draw ratio and corresponding frequency at criticality as a function of the Deborah number for the UCM model. The obtained results are in good agreement with the ones presented earlier by Silagy et al. [5]. As shown by Denn et al. [24], no steady state solutions exist for  $Dr \leq 1 + D\epsilon^{-1}$ , where the equality corresponds to the case where the fluid traveling time from inlet to outlet is approximately equal to the relaxation time. This is resulting from the high stresses predicted by the UCM model for large relaxation times and strain rates. The corresponding region is shaded gray in Fig. 6.

Besides a very small stability minimum, visualized in the inset of Fig. 6, the UCM model predicts a purely stabilizing influence of elasticity, i.e., increasing  $D\epsilon$ . At  $D\epsilon_c = 0.013$ , the neutral stability curve exhibits a fold point, leading to unconditional stability for  $D\epsilon > D\epsilon_c$ , and to a second critical draw ratio for  $D\epsilon < D\epsilon_c$ , above which the system becomes stable again. The frequency at criticality  $\omega_{I,c}$  follows the same qualitative trend as  $Dr_c$ . The second critical draw ratio, however, has never been observed experimentally [1], and it is shown below that the drastic increase of  $Dr_c$  can be directly correlated to the unphysical divergence of the elongational viscosity of the UCM model.

#### 4.4. Giesekus model

As visualized by Fig. 7, the Giesekus model predicts a mostly destabilizing effect of increasing elasticity, i.e., increasing Deborah number. For small values

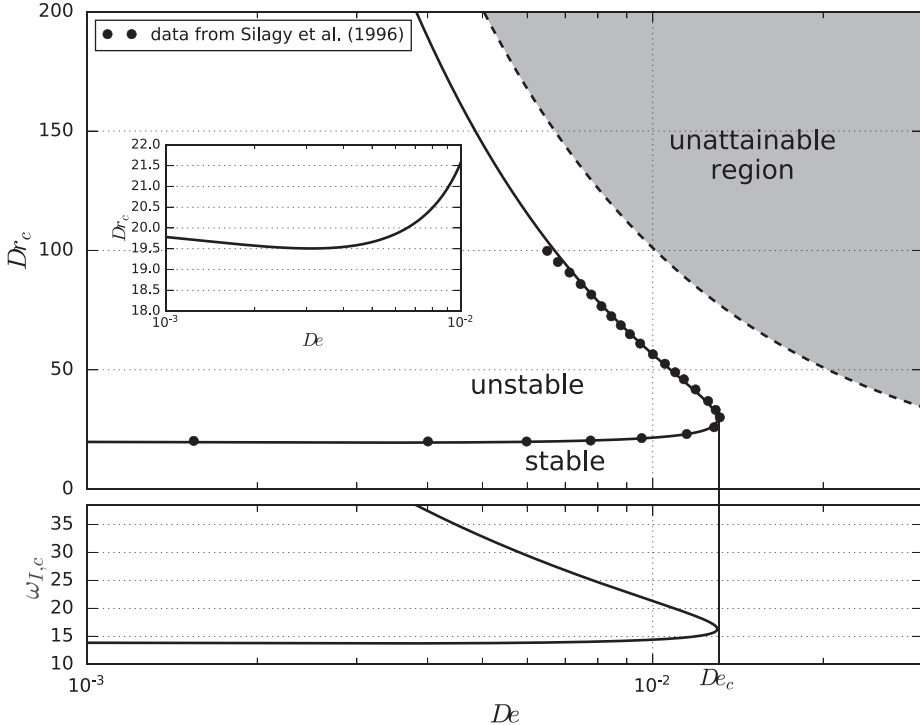


Figure 6: Critical draw ratio (top) and frequency at criticality (bottom) as a function of the Deborah number for the UCM model as obtained by numerical continuation, and comparison with the data of Silagy et al. [5]. The system becomes unconditionally stable for  $De > De_c = 0.013$  and a small stability minimum is located at  $De = 3.1 \times 10^{-3}$  (see inset). No steady state solutions exist in the unattainable region.

of  $\alpha \lesssim 0.1$ , a distinct stability maximum can be observed, while the critical draw ratio decreases monotonically with increasing  $De$  for larger values of  $\alpha$ . The only exception is  $\alpha = 0.9$ , where a small stability minimum around  $De \approx 0.5$  is found. In particular, the spectral analysis for  $\alpha = 0.9$  reveals a domain of  $De$  within which the second instability mode with higher frequency becomes unstable first. The two insets showing the first five complex pairs of eigenvalues at different configurations visualize this effect of leading mode switching, which implies a non-continuous jump in the frequency at criticality  $\omega_{I,c}$ , depicted as well in Fig. 7. Apart from that, the frequency exhibits the same qualitative trend as the critical draw ratio for all values of  $\alpha$ . In the Newtonian limit of small Deborah numbers, all curves converge to  $Dr_c = 20.218$  and  $\omega_{I,c} = 14.11$ , as expected. In the elastic limit of large Deborah numbers, the curves approach again a common value of  $Dr_c = 5.6$  and  $\omega_{I,c} = 10.5$ .

As can be seen by the right inset in Fig. 7, the real parts of the first two eigenvalues are very close and as a result, the error in  $Dr_c$  introduced by following exclusively the first mode, as done in numerical continuation, is negligible. The

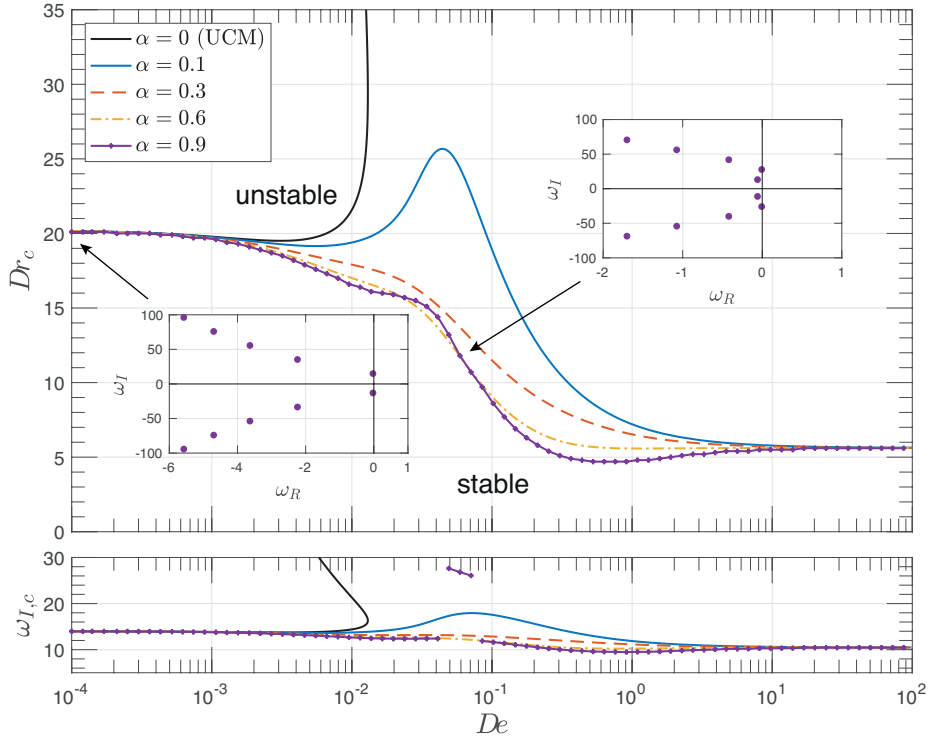


Figure 7: Critical draw ratio (top) and frequency at criticality (bottom) as a function of the Deborah number for the Giesekus model for  $\alpha = 0, 0.1, 0.3, 0.6, 0.9$ . The insets show the eigenvalues of the most unstable modes for  $De = 10^{-4}$  (left) and  $De = 0.06$  (right) for  $\alpha = 0.9$ .

jump in frequencies, however, is significant and can be an indicator of a change in the mechanism underlying the instability. As typical values for the Giesekus model for  $\alpha$  are rather below 0.5, we will not further investigate this issue in this work, merely noting that viscoelasticity can in general lead to switching of the most unstable mode of draw resonance. In general, increasing the nonlinear parameter  $\alpha$  appears to have a destabilizing effect, with a small exception for  $0.01 < De < 0.1$ , where the neutral stability curves intersect for large values of  $\alpha$ .

#### 4.5. PTT model

The stability predictions of the PTT model, as visualized by Fig. 8, are in qualitative agreement with those of the Giesekus model. Increasing the Deborah number has a primarily destabilizing effect. For small values of the nonlinear parameter  $\varepsilon \lesssim 0.1$ , a stability maximum occurs between  $De = 0.01$  and 0.1. In the elastic limit of high Deborah numbers, all neutral stability curves converge to common values  $Dr_c = 1.6$  and  $\omega_{I,c} = 6.7$ , i.e., a lower critical draw ratio and frequency as compared to the Giesekus model predictions. Increasing  $\varepsilon$  always leads to destabilization for all Deborah numbers.

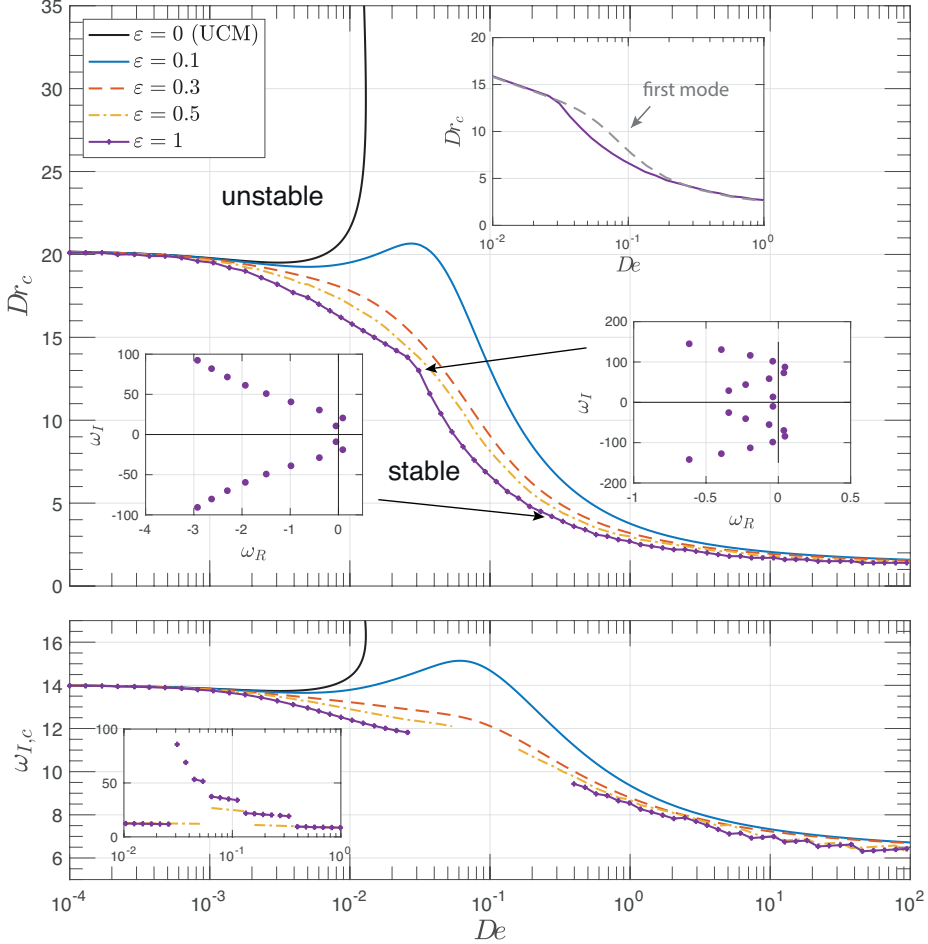


Figure 8: Critical draw ratio (top) and frequency at criticality (bottom) as a function of the Deborah number for the PTT model for  $\varepsilon = 0, 0.1, 0.3, 0.5, 1$ . Two insets show the eigenvalues of the most unstable modes for  $D\!e = 0.03$  (right bottom) and  $D\!e = 0.28$  (left) for  $\varepsilon = 1$ . A third inset (right top) compares the critical draw ratio to the prediction following only the first instability mode.

Similar to the Giesekus model, but more pronounced is the effect of leading mode switching for  $\varepsilon \gtrsim 0.5$ . For  $\varepsilon = 1$ , we find that one of the first six instability modes can become the most unstable one (see bottom insets in Fig. 8 (top)), leading to a change in frequency up to a factor of 7, which is also shown by the inset of Fig. 8 (bottom). In contrast to the Giesekus model, this mode switching also leads to a significant change in the critical draw ratio, as depicted by the top inset in Fig. 8 (top). Christodoulou et al. [19] also observed switching of the most unstable instability mode in their analysis of a multi-relaxation-mode PTT model.

## 5. Generalized Newtonian fluid models

### 5.1. Effective elongational viscosity

Generalized Newtonian fluid (GNF) models can offer an efficient way to cover the main aspects of viscoelastic fluids, if (non-Newtonian) viscous effects are dominating and purely elastic effects are negligible. In this case, the viscosity is assumed to be a function of the flow properties, mostly the deformation rate. Instead of the shear viscosity  $\eta$ , we use here the steady effective elongational viscosity  $\tilde{\mu}_s$  as defined by Eq. (26), as film casting is dominated by elongational deformation.

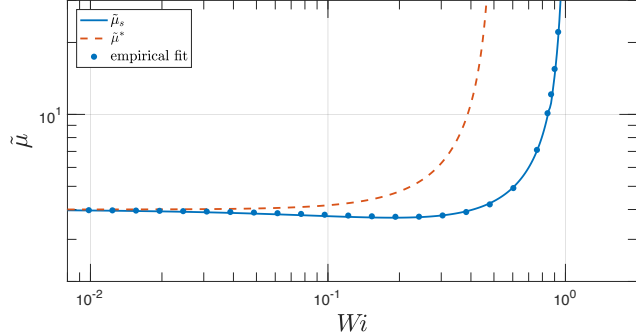
We evaluate  $\tilde{\mu}_s$  for all three models for various values of  $Dr$  and  $De$ . Analogue to the transversal stress component shown by Fig. 5, the effective elongational viscosity appears to be independent of the draw ratio and different configurations yield parts of a common mastercurve, which can be interpolated numerically. Using the empirical boundary condition (24), the boundary layer effects close to the die, similar to the ones found for the transversal stress (Fig. 4), can be observed. These effects disappear if the interpolated mastercurve is used as initial stress boundary condition instead.

Figure 9 depicts the resulting effective elongational viscosities for all three models as a function of  $Wi$ , evaluated using  $\partial_x u_s$ , and compares them to the steady planar elongational viscosity at constant strain rate,  $\tilde{\mu}^*$ . For all three models, the shape of  $\tilde{\mu}_s$  is very similar to  $\tilde{\mu}^*$ . There is, however, a quantitative difference, which is crucial for the draw resonance behavior as shown below. In general it can be stated that the strain hardening effect is diminished as compared to the constant strain rate deformation. In the case of the UCM model, a small viscosity minimum can be observed and the curve diverges at a larger Weissenberg number close to unity. For the Giesekus model, all plateau values for large Weissenberg numbers are lowered and a significant strain hardening is present only for small values of  $\alpha$ . Similarly, the strain hardening maximum predicted by the PTT model becomes less pronounced and vanishes for instance already for  $\varepsilon = 0.3$ , being still present for  $\tilde{\mu}^*$ .

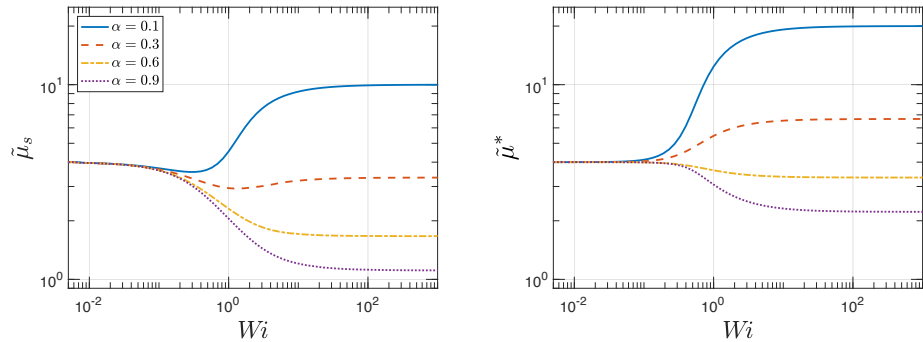
Comparing now the effective elongational viscosity curves with the neutral stability curves shown in Figs. 6-8 reveals strong similarities. In the case of the UCM model, the small viscosity minimum, which is not present for  $\tilde{\mu}^*$ , and the sharp strain hardening both resemble of the small stability minimum and the overall stabilizing influence of elasticity. In the case of the Giesekus and PTT models, it is striking that a stability maximum is present if and only if the corresponding effective elongational viscosity exhibits strain hardening. Note that this is not true for the planar viscosity at constant shear rate, which for instance shows strain hardening as well for  $\alpha = 0.3$  or, respectively,  $\varepsilon = 0.3$ , where increasing  $De$  has a purely destabilizing effect.

These observations strongly suggest that the effective elongational viscosity plays a key role in the dynamical behavior and in particular in the stability of the process. For this reason, we will analyze in the following the steady state and instability behavior of GNF models based on the effective elongational viscosity and compare the results to the full viscoelastic model predictions. For the sake

(a)



(b)



(c)

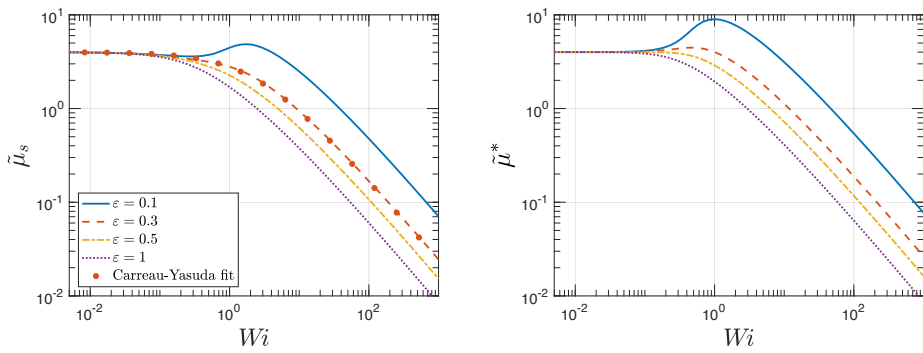


Figure 9: Effective viscosities at steady state  $\tilde{\mu}_s$  for the (a) UCM (b) Giesekus and (c) PTT models. In all three cases, the quantity appears to depend solely on the Weissenberg number  $Wi$  and the shapes of the curves resemble the planar elongational viscosities at constant strain rate,  $\tilde{\mu}^*$ , which are depicted as well for comparison. For the UCM model and the PTT model ( $\varepsilon = 0.3$ ), empirical fits with Eqs. (30) and (35), respectively, are indicated.

of compactness, we focus primarily on the UCM and PTT models and refer to the Giesekus model merely in a qualitative way at the end of the section.

### 5.2. Reproducibility of UCM and PTT results using GNF models

#### 5.2.1. UCM model

We fit an empirical function to the effective elongational viscosity obtained for the UCM model in order to use it in a GNF model. The employed expression is inspired by the analytical solution of the planar elongational viscosity at constant strain rate and given by

$$\tilde{\mu}_M(Wi) = \left( \frac{2 + p_2}{1 - p_0 Wi} + \frac{2 - p_2}{1 + p_1 Wi} \right), \quad (30)$$

with the free parameters determined as  $p_0 = 1.0$ ,  $p_1 = 1.64$ , and  $p_2 = -0.56$ . The corresponding fit is shown in Fig. 9(a) and exhibits good agreement with the numerical data. While the effective viscosity is originally obtained exclusively from the steady state solution, the main assumption of the GNF model now is that this viscosity is valid as well for time dependent dynamics. The GNF model is thus given by Eqs. (16) and (17), supplemented by

$$\nu = \tilde{\mu}_M(Wi) \partial_x u. \quad (31)$$

Following the previously introduced steps of the linear stability analysis and recalling that  $Wi = De \partial_x u$  for dimensionless quantities, the steady state equations read

$$u'_s = \frac{2\nu_s}{4 + \sqrt{16 + De \nu_s (p_0 + p_1) (4p_2 + De (p_0 + p_1) \nu_s)}}, \quad (32a)$$

$$h'_s = -\frac{h_s}{u_s} u'_s, \quad (32b)$$

$$\nu'_s = -\frac{\nu_s}{h_s} h'_s, \quad (32c)$$

and the perturbation equations are given by

$$U' = \frac{\nu_s (1 - p_0 De u'_s)^2 (1 + p_1 De u'_s)^2}{d} N - \frac{u'_s}{u_s} U, \quad (33a)$$

$$H' = -\left( \omega \frac{H}{u_s} + U \right), \quad (33b)$$

$$N' = -H', \quad (33c)$$

with

$$d = 4u_s \left[ 1 - De u'_s \left( \left( 1 - \frac{p_2}{2} \right) \left( 1 - De u'_s \frac{p_0}{2} \right) p_0 - \left( 1 + \frac{p_2}{2} \right) \left( 1 + De u'_s \frac{p_1}{2} \right) p_1 \right) \right]. \quad (34)$$

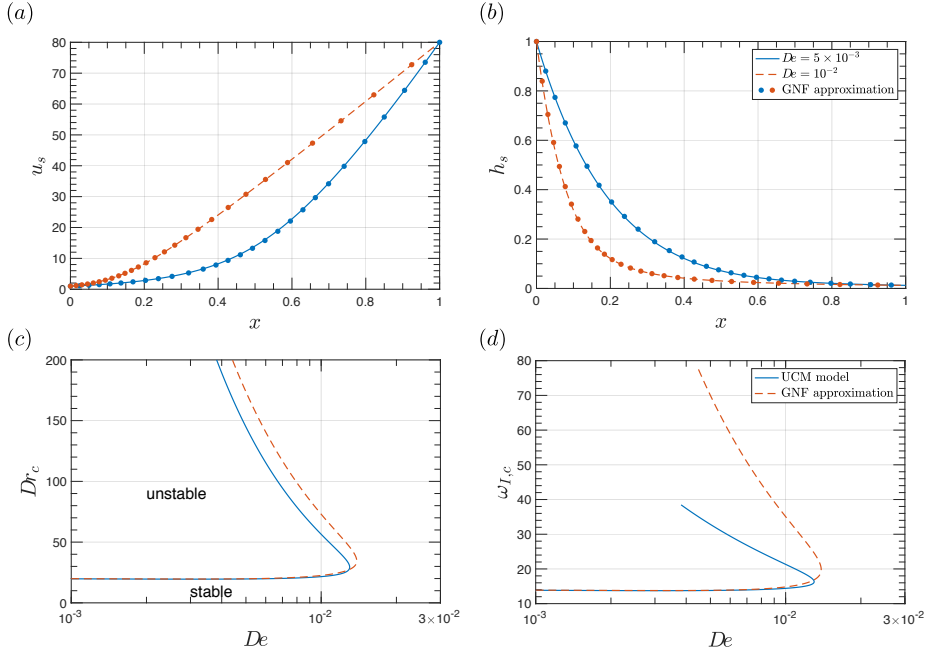


Figure 10: Comparison between the UCM model and its GNF approximation based on the effective elongational viscosity, which is modeled by Eq. (30). (a,b) Steady state solutions for axial velocity  $u_s$  and film thickness  $h_s$  for  $De = 5 \times 10^{-3}, 10^{-2}$  and  $Dr = 80$ . (c) Critical draw ratio. (d) Frequency at criticality.

Figures 10(a,b) compare the steady states of axial velocity and film thickness as obtained from this GNF approximation to the results of the UCM model for two values of the Deborah number and  $Dr = 80$ . As expected due to the high accuracy of the empirical fit, both models yield practically identical stationary solutions. The neutral stability curves resulting from both models are shown in Fig. 10(c). The qualitative shape remains the same, and the quantitative offset of the GNF approximation after the fold point appears to be small. The mismatch becomes more pronounced, however, in the frequency at criticality  $\omega_{I,c}$ , which is shown in Fig. 10(d). Still, the qualitative coincidence and the moderate discrepancy suggests that the essential mechanism underlying the stability behavior of the UCM model is well captured by the GNF approximation. This strongly indicates that the stability is primarily governed by the effective elongational viscosity, which, however, in the case of the UCM model, is known to be unphysical due to the excessive strain hardening finally leading to divergent behavior. For this reason, it is highly unrecommended to apply the UCM model for stability studies on film casting or fiber spinning.

### 5.2.2. PTT model

For cases of the PTT model with no strain hardening prediction, it is possible to fit the effective elongational viscosity with the expression of the Carreau-Yasuda (CY) model [29], which is given by

$$\tilde{\mu}_{\text{cy}}(Wi) = \frac{4}{[1 + (k Wi)^m]^{\frac{1-n}{m}}}. \quad (35)$$

For  $\varepsilon = 0.3$ , the free parameters are determined as  $k = 0.433$ ,  $n = 0.162$ , and  $m = 0.889$  and the corresponding fit is shown in Fig. 9(c). Due to the particular structure of Eq. (35), it is impossible to analytically solve the GNF model equation for  $\partial_x u$ , as it occurs with various exponents in the model equations. For this reason, we use  $\partial_x u$  instead of  $\nu$  as a variable, which leads to the following steady state equations,

$$u_s'' = \frac{u_s'^2 (1 + k De u_s')^m}{u_s c}, \quad (36a)$$

$$h_s' = -\frac{h_s}{u_s} u_s', \quad (36b)$$

with the auxiliary variable

$$c = (1 + n (k De u_s'))^m. \quad (37)$$

The perturbation equations read

$$U'' = \frac{1}{u_s^2 c^2} [m(1-n) (k De u_s')^m u_s'^2 U + \omega c (1 + (k De u_s')^m) u_s' H + (1-n) (k De u_s')^m (m+2c) u_s u_s' U'], \quad (38a)$$

$$H' = -\left(\omega \frac{H}{u_s} + U\right). \quad (38b)$$

Similar to the previously discussed case of the UCM model, the steady state solutions of the GNF approximation shown in Figs. 11(a,b) agree very well with the PTT model results. Small deviations are most likely caused by imperfections in the fitting of the CY model. The neutral stability curves (Fig. 11(c)), however, coincide only for  $De < 0.1$ . For larger Deborah numbers, the GNF approximation overpredicts the critical draw ratio and finally diverges at  $De \approx 0.5$ , while the PTT model predicts a monotonically decreasing stability with increasing  $De$ . Note that the divergent behavior is not caused by a switch of the most unstable mode, as it occurs for the Giesekus and PTT models as discussed above, as higher modes of instability were checked separately. Moreover, the predicted frequency at criticality of the GNF approximation is in good coincidence with the PTT model result until the point of divergence (see Fig. 11(d)).

This reveals that the use of GNF models for studying the stability is limited at least to rather low Deborah numbers. In the case of the UCM model, this is

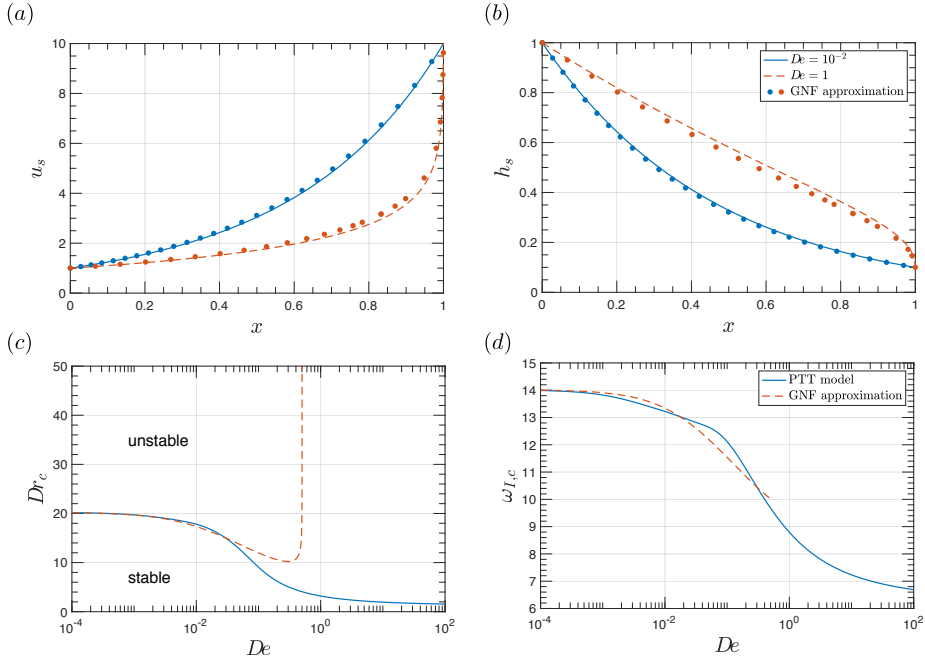


Figure 11: Comparison between the PTT model,  $\varepsilon = 0.3$ , and its GNF approximation based on the effective elongational viscosity, which is modeled by the CY Eq. (35). (a,b) Steady state solutions for axial velocity and film thickness for  $De = 10^{-2}$  and 1 and  $Dr = 10$ . (c) Critical draw ratio. (d) Frequency at criticality.

not directly seen as the neutral stability curve does not exceed the regime of low  $De$ . A likely reason for this limitation is the missing explicit time dependence of the stress tensor, which appears in the viscoelastic models applied here in the form of the upper-convected time derivative. As a consequence, there exists an additional, yet unexplored mechanism underlying the stability behavior of systems dominated by elastic effects. The presence of such a mechanism is also visible in the stability results of the Giesekus model (Fig. 7): While the effective elongational viscosity reaches a plateau value in the elastic limit of large  $Wi$  (Fig. 9(b)), the corresponding critical draw ratio is clearly below the Newtonian limit value of  $Dr_c = 20.218$ .

## 6. Influence of strain hardening and strain thinning

Besides this purely elastic effect, the mechanism underlying the (de-)stabilization of non-Newtonian, viscous properties is still unclear. In particular, the question arises why a purely strain thinning material leads to a non-monotonous stability behavior, including a diverging critical draw ratio, as shown in Fig. 11(c)). There exists an explanation for a viscous mechanism underlying draw resonance, which is based on the work of Kim et al. [30] and was later refined [7, 6, 26]. The

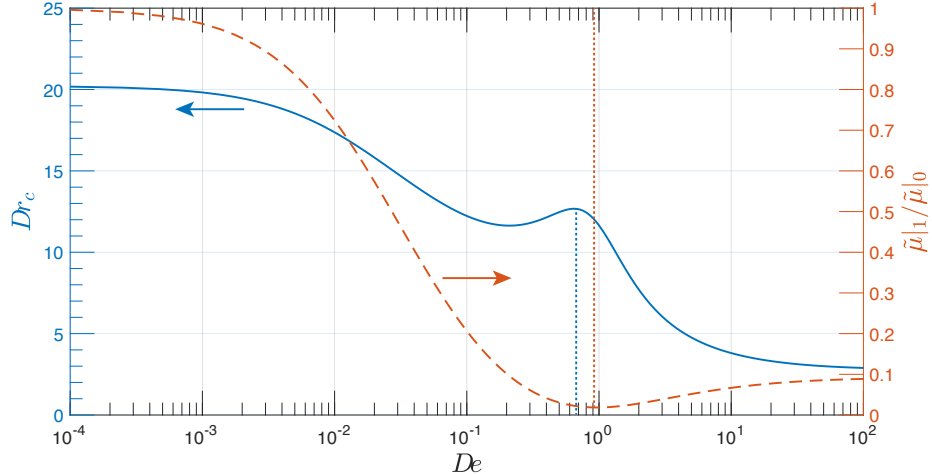


Figure 12: Neutral stability curve of the CY model for  $n = 0.3$ ,  $m = 1$ , and  $k = 1$  (blue, solid), together with the ratio of effective elongational viscosities at outlet to inlet (orange, dashed). The dotted lines indicate the extrema of the two curves.

general idea is to follow the propagation of an initial perturbation of the tension  $f = h\nu$ . According to Eq. (17), this tension is constant along  $x$ . Evaluation of the continuity equation (16) at  $x = 0$ , where  $h$  is time independent and equal to unity, enables us to write

$$\partial_x h|_0 = -\frac{f}{\tilde{\mu}|_0}, \quad (39)$$

where the GNF model expression  $\nu = \tilde{\mu} \partial_x u$  for the normal stress difference was used. This equation reveals that a perturbation of the tension, e.g., at the outlet, instantaneously leads to a perturbation in thickness at the inlet, which then travels downwards, finally causing another perturbation at the outlet and closing the loop of the feedback mechanism. Exploiting the fact that  $f$  is constant in space, we can rewrite Eq. (39) to better visualize the relation between perturbations at in- and outlet:

$$\partial_x h|_0 = -\frac{\tilde{\mu}|_1}{\tilde{\mu}|_0} h|_1 \partial_x u|_1. \quad (40)$$

Further analysis of the CY model reveals that the neutral stability curve in fact does not always diverge, but exhibits for some parameter combinations merely a stability maximum with an overall destabilizing trend for increasing Deborah number. An example is shown in Fig. 12, where  $m = k = 1$  and  $n = 0.3$ , and where a stability maximum occurs close to  $De = 1$ . Note that  $n$  tunes the slope of the power-law regime for  $k Wi \ll 1$ , while  $m$  sets the sharpness of the transition from Newtonian to power-law behavior. The shown case here

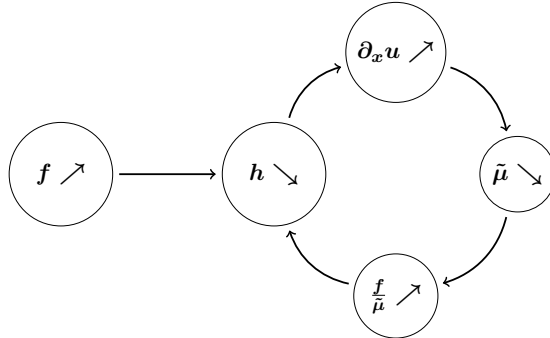


Figure 13: Visualization of the dynamic mechanism underlying the destabilizing effect of strain thinning. While  $f$  is constant in space, all other quantities correspond to a position close to the inlet.

basically differs from the one fitted to the PTT viscosity above in the value of  $n$ , leading to a less steep power-law slope.

Following Eq. (40), we now look at the ratio of effective elongational viscosities at outlet to inlet, as this is the quantity which differs from the Newtonian case. It is plotted in Fig. 12 as well and exhibits a local minimum close to the stability maximum. With the viscous stability mechanism described above in mind, Eq. (40) can be interpreted in the following way. While a perturbation at the outlet leads to a perturbation at the inlet, this effect is scaled by the ratio of effective viscosities. This seems to be reasonable as the mechanism is based on the perturbation of tension, which is proportional to the viscosity. Therefore, a perturbation at the outlet has less effect on the perturbation at the inlet, if the viscosity at the inlet is larger as compared to the outlet. If the ratio of viscosities is below a threshold, the instability is completely suppressed and the critical draw ratio diverges, as observed in Fig. 11(c). Note that a similar argumentation was already successfully used in the past to explain the change in stability behavior caused by the neck-in in film casting [6].

As we are employing merely the steady states of the elongational viscosities in this reasoning, we call this mechanism the “static mechanism” underlying non-Newtonian draw resonance. However, according to this explanation one would expect a purely stabilizing effect of a strain thinning fluid like the analyzed one, as the strain rate is expected to increase along  $x$  during the casting and the thinning effect is more pronounced for larger  $De$ . Instead, the overall trend appears to be destabilizing with increasing  $De$  and it is known that pure power-law models lead to an increase/decrease of  $Dr_c$  for strain hardening/thinning materials [9]. For this reason, there has to exist a second mechanism, which we will call the “dynamic mechanism”.

The dynamic mechanism is visualized in Fig. 13 for a strain thinning material and can be understood as follows. According to Eq. (39), a perturbation of the tension, e.g., a temporary increase, leads to a stronger (negative) gradient of the film thickness at the inlet and therefore to a smaller film thickness close to

the inlet. Due to continuity, this increases the velocity and thus the strain rate close to the inlet as well. For a strain thinning/hardening material, this has the consequence of a decreasing/increasing effective viscosity, which in turn leads to an increase/decrease of the ratio on the right-hand side of Eq. (39), which finally amplifies/damps the initial effect. Therefore, the dynamic mechanism leads to a destabilization/stabilization of strain thinning/hardening, while the static mechanism has an opposing effect.

Whether the static or the dynamic mechanism is more dominant and governs the stability behavior depends on the particular shape of the effective elongational viscosity. For pure power-law behavior, the dynamic mechanism is clearly stronger, but in the case of the CY model, the situation is more subtle. As long as the ratio of outlet to inlet effective viscosity does not deviate too much from unity, the dynamic mechanism is more pronounced than the static. If, however, the material at the inlet is rather governed by the Newtonian plateau regime, while the material at the outlet enters already the power-law regime, the non-Newtonian effect close to the inlet and thus the dynamic mechanism is weak compared to the static mechanism, and the stability behavior changes qualitatively.

It should be noted that it was separately verified that a time-independent GNF model, which depends on the steady state of the strain rate only, yields indeed a purely stabilizing/destabilizing effect for strain thinning/hardening materials, as the dynamic mechanism is absent here. A similar effect was observed by Scheid et al. [7], when they found that cooling can have a destabilizing effect if the Stanton number is very large so that the material temperature is actually completely governed by the ambient temperature and therefore time independent.

## 7. Conclusions and Outlook

We studied the influence of viscoelastic, and in particular non-Newtonian, effects on the draw resonance instability in film casting. For this purpose, a comprehensive framework for a linear stability analysis of the UCM, Giesekus, and PTT models was derived. The boundary condition for the initial stress was chosen in a way that a deformation history caused by a particular flow inside the die is excluded from the analysis, which is consistent with the free boundary condition method of Papanastasiou et al. [22]. While the UCM model is known to predict a strong stabilizing effect of elasticity, more sophisticated models like the Giesekus and the PTT model show an overall destabilizing trend. This qualitative difference could be related to the unphysical, diverging elongational viscosity of the UCM model. For this reason, the UCM model is highly unrecommended for studies of viscoelastic film casting or related processes like fiber spinning. For large values of the nonlinear parameters of the Giesekus and the PTT model, a switch of the most unstable mode, and thus a discrete change of the frequency at criticality can be observed.

While it is possible for low values of the Deborah number to reproduce the results of the viscoelastic models using GNF models based on the effective

elongational viscosity, which was introduced as a key quantity for the analysis, this approximation fails if elastic effects become too pronounced. Nevertheless, the GNF models, in particular the CY model, enable us to shed light on the two opposing mechanisms underlying the effects of strain hardening and thinning materials on the stability.

Apart from new insights in non-Newtonian effects in draw resonance, the present results strongly indicate the existence of an additional, purely elastic stability mechanism. Besides the failure of the GNF approximation for high Deborah numbers, a change in the basic mechanism can also be indicated by the observed switching of the most unstable instability mode. Given that the common approaches to explain draw resonance are based on a viscous material, the question arises whether we can still speak of draw resonance in the high elastic regime, or whether this is another type of instability. This is similar to the transition from draw resonance to the Rayleigh-Plateau instability when surface tension in fiber spinning is increased [26]. In a weakly nonlinear stability analysis, Gupta and Chokshi [14] found a transition from a supercritical to a subcritical instability if the Deborah number exceeds a threshold value, which is another hint for this hypothesis. However, it has to be noted that this analysis is at least partially wrong, as pointed out by Gallaire et al. [31]. Further work on the nature of the elastic instability is therefore needed, and it is hoped that the present study can help hereby as a solid basis.

### Acknowledgments

The author thanks Manuel Alves, François Gallaire, Rob Poole, and Benoit Scheid for fruitful discussions and useful tips.

### References

- [1] S. G. Hatzikiriakos, K. Migler, *Polymer processing instabilities*, Dekker, New York, 2005.
- [2] Y. L. Yeow, On the stability of extending films: a model for the film casting process, *Journal of Fluid Mechanics* 66 (1974) 613–622.
- [3] F. Cao, R. E. Khayat, J. Puskas, Effect of inertia and gravity on the draw resonance in high-speed film casting of Newtonian fluids, *International Journal of Solids and Structures* 42 (2005) 5734–5757.
- [4] M. Bechert, D. W. Schubert, B. Scheid, Practical mapping of the draw resonance instability in film casting of Newtonian fluids, *European Journal of Mechanics - B/Fluids* 52 (2015) 68–75.
- [5] D. Silagy, Y. Demay, J.-F. Agassant, Study of the stability of the film casting process, *Polymer Engineering & Science* 36 (1996) 2614–2625.

- [6] M. Bechert, D. W. Schubert, B. Scheid, On the stabilizing effects of neck-in, gravity, and inertia in Newtonian film casting, *Physics of Fluids* (1994-present) 28 (2016) 024109.
- [7] B. Scheid, S. Quiliggotti, B. Tran, R. Gy, H. A. Stone, On the (de)stabilization of draw resonance due to cooling, *Journal of Fluid Mechanics* 636 (2009) 155–176.
- [8] J. A. Pearson, Y. T. Shah, On the stability of isothermal and nonisothermal fiber spinning of power-law fluids, *Industrial & Engineering Chemistry Fundamentals* 13 (1974) 134–138.
- [9] G. R. Aird, Y. L. Yeow, Stability of film casting of power-law liquids, *Industrial & Engineering Chemistry Fundamentals* 22 (1983) 7–10.
- [10] R. Van der Hout, Draw resonance in isothermal fibre spinning of Newtonian and power-law fluids, *European Journal of Applied Mathematics* 11 (2000) 129–136.
- [11] J. S. Lee, D. M. Shin, H. W. Jung, J. C. Hyun, Stability analysis of a three-layer film casting process, *Korea-Australia Rheology Journal* 19 (2007) 27–33.
- [12] D. Shin, J. Lee, J. Kim, H. Jung, J. Hyun, Transient and steady-state solutions of 2D viscoelastic nonisothermal simulation model of film casting process via finite element method, *Journal of Rheology* 51 (2007) 393–407.
- [13] C. van der Walt, M. Hulsen, A. Bogaerds, H. Meijer, M. Bulters, Stability of fiber spinning under filament pull-out conditions, *Journal of Non-Newtonian Fluid Mechanics* 175-176 (2012) 25–37.
- [14] K. Gupta, P. Chokshi, Weakly nonlinear stability analysis of polymer fibre spinning, *Journal of Fluid Mechanics* 776 (2015) 268–289.
- [15] O. Zavinska, J. Claracq, S. van Eijndhoven, Non-isothermal film casting: Determination of draw resonance, *Journal of Non-Newtonian Fluid Mechanics* 151 (2008) 21–29.
- [16] T. I. Burghela, H. J. Grieß, H. Münstedt, An in situ investigation of the draw resonance phenomenon in film casting of a polypropylene melt, *Journal of Non-Newtonian Fluid Mechanics* 173-174 (2012) 87–96.
- [17] V. R. Iyengar, A. Co, Film casting of a modified Giesekus fluid: a steady-state analysis, *Journal of Non-Newtonian Fluid Mechanics* 48 (1993) 1–20.
- [18] V. R. Iyengar, A. Co, Film casting of a modified Giesekus fluid: Stability analysis, *Chemical engineering science* 51 (1996) 1417–1430.

- [19] K. Christodoulou, S. G. Hatzikiriakos, D. Vlassopoulos, Stability Analysis of Film Casting for PET Resins Using a Multimode Phan-Thien-Tanner Constitutive Equation, *Journal of Plastic Film and Sheeting* 16 (2000) 312–332.
- [20] R. Dhadwal, S. Banik, P. Doshi, H. Pol, Effect of viscoelastic relaxation modes on stability of extrusion film casting process modeled using multimode Phan-Thien-Tanner constitutive equation, *Applied Mathematical Modelling* 47 (2017) 487–500.
- [21] R. G. Larson, *Constitutive Equations for Polymer Melts and Solutions: Butterworths Series in Chemical Engineering*, Butterworth-Heinemann, 1988.
- [22] T. C. Papanastasiou, V. D. Dimitriadis, L. E. Scriven, C. W. Macosko, R. L. Sani, On the inlet stress condition and admissibility of solution of fiber-spinning, *Advances in Polymer Technology* 15 (1996) 237–244.
- [23] E. Doedel, A. Champneys, T. Fairgrieve, Y. Kuznetsov, B. Sandstede, X. Wang, AUTO97 continuation and bifurcation software for ordinary differential equations., AUTO software is freely distributed on <http://indy.cs.concordia.ca/auto/>, 1997.
- [24] M. M. Denn, C. J. Petrie, P. Avenas, Mechanics of steady spinning of a viscoelastic liquid, *AIChE Journal* 21 (1975) 791–799.
- [25] T. Barborik, M. Zatloukal, C. Tzoganakis, On the role of extensional rheology and Deborah number on the neck-in phenomenon during flat film casting, *International Journal of Heat and Mass Transfer* 111 (2017) 1296–1313.
- [26] M. Bechert, B. Scheid, Combined influence of inertia, gravity, and surface tension on the linear stability of Newtonian fiber spinning, *Physical Review Fluids* 2.
- [27] M. Renardy, Draw Resonance Revisited, *SIAM Journal on Applied Mathematics* 66 (2006) 1261–1269.
- [28] T. A. Driscoll, N. Hale, L. N. Trefethen, *Chebfun Guide*, 2014.
- [29] C. W. Macosko, *Rheology: Principles, Measurements, and Applications*, Wiley-VCH, New York, 1994.
- [30] B. M. Kim, J. C. Hyun, J. S. Oh, S. J. Lee, Kinematic waves in the isothermal melt spinning of Newtonian fluids, *AIChE journal* 42 (1996) 3164–3169.
- [31] F. Gallaire, E. Boujo, V. Mantic-Lugo, C. Arratia, B. Thiria, P. Meliga, Pushing amplitude equations far from threshold: application to the supercritical Hopf bifurcation in the cylinder wake, *Fluid Dynamics Research* 48 (2016) 061401.